ACS OMEGA

http://pubs.acs.org/journal/acsodf

Article

Synthesis and Characterization of rGO@ZnO Nanocomposites for Esterification of Acetic Acid

Fahad A. Alharthi,*,† Amjad Abdullah Alsyahi, Saad G. Alshammari, Hessah A. AL-Abdulkarim,† Amal AlFawaz, and Ali Alsalme

Cite This: *ACS Omega* 2022, 7, 2786−2797

Read Online

ACCESS | Metrics & More | Article Recommendations

ABSTRACT: In the present work, the aim is to synthesize reduced graphene oxide (rGO) and zinc:reduced graphene oxide composite catalysts (ZnO:rGO) for esterification of acetic acid with *n*-heptanol. The physical and chemical characteristics of the rGO and rGO-metal oxide composite catalysts such as textural surface characteristics, surface morphology, thermal stability, functional groups, and elemental analysis were studied. The surface areas of rGO, $ZnO_{(0.5\ M)}$, and $ZnO_{(1\ M)}$ were recorded, respectively, at 31.72, 27.65, and 36.19 $m^2\ g^{-1}$. Furthermore, esterification reaction parameters such as the reaction time, catalyst dosage, and reaction temperature for acetic acid were optimized to check the feasibility of rGO-metal oxide composites for a better conversion percentage of acetic acid. The optimized catalyst was selected for further optimization, and the optimum reaction parameters found were 0.1 wt % of catalyst, 160 min reaction duration, and 100 °C reaction temperature with a maximal yield of 100%. At 110 °C, the reaction conducted in the presence of 0.1 g of catalyst displayed more yield than the uncatalyzed reaction.

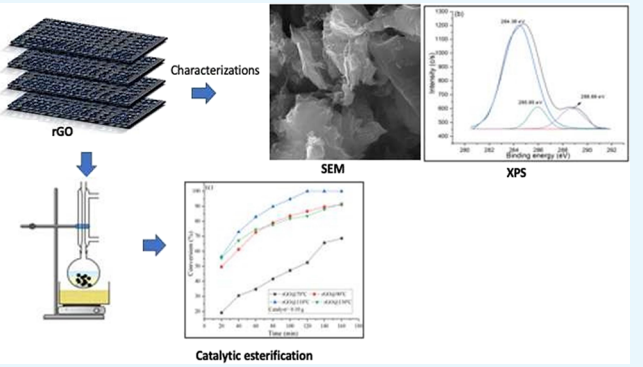

1. INTRODUCTION

Energy sustainability will be one of the challenges for the next 40 years due to the rapid exhaustion of fossil fuel reserves for continuous energy generation demands.[1] Esters are one of the examples of alternative energy sources that are sustainable, renewable, and nontoxic due to fact that they can be synthesized with edible or inedible oils.[2] In addition, esters possess a high cetane value, flash point, and similar lubricity to conventional diesel wherein it can perform in the diesel engine without a need for modification.[3]

Esters can be produced though catalytic esterification of fatty acids and alcohols in the presence of acidic catalysts. Strong acidic catalysts such as sulfuric acid, phosphoric acid, hydrochloric acid, perchlorous acid, and nitric acid work with high FFA and water content of low-quality feedstocks such as waste cooking oil, Jatropha oil,[4] palm fatty acid distillate (PFAD),[5] lard oil,[6] and animal fats.[7] However, these homogeneous catalysts are not available for recovery and recycle as well as they create wastewater upon biodiesel purification and are corrosive toward reactors over a longer time.[8] As a solution, a solid acid catalyst has been introduced to overcome the stated problems by providing an environmentally friendly and cost-effective alternative with better catalyst recovery and reusability.[9]

Over the past two decades, various types of solid acid catalysts have been produced for catalytic esterification, for instance, nanosized metal-based catalysts,[10] zeolites, sulfonate resins, sulfonated carbon-based catalysts, and sulfonated oxide catalysts. These solid catalysts are designated with different structural properties that would influence the catalytic performances by having specific active sites for the reaction to take place between the reactants.[11,50] For example, $ZnAl_2O_4$-SO_3H possessed a high surface area of 352.39 $m^2\ g^{-1}$ and high acid density of 1.95 mmol g^{-1} and successfully esterified 95% PFAD-based biodiesel.[12] Saba et al. prepared a zeolite precursor-impregnated KOH catalyst (KOH/ZSM5) for producing biodiesel from sunflower oil that was reused for three consecutive runs with >90% yield before catalyst deactivation due to active site leaching.[13] A Nafion/silica composite (SAC-13) was utilized for a triglyceride hydrolysis-esterification reaction of FFA and was regenerated for four reusability cycles by methanol washing.[14] Catalyst deactivation

Received: October 6, 2021
Accepted: December 24, 2021
Published: January 14, 2022

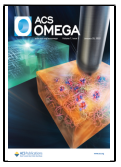

ACS Publications

© 2022 The Authors. Published by American Chemical Society

https://doi.org/10.1021/acsomega.1c05565
ACS Omega 2022, 7, 2786−2797

tends to happen after consecutive times of catalyst reusability, especially toward metal-based nanocatalysts due to weak metal bonding, among which the nanoparticles are allowed to aggregate and clump.[15,16] Considering that carbon-based catalysts derived from waste biomass provide sustainability and cost savings for ester production, they have attracted the interest of researchers. The waste carbon material can be transformed into activated carbon and derived as a catalyst support.[17] The activated carbon support provides high stability[18] and a large surface area with a specific pore diameter for active site attachment[19] and is easy to functionalize by undergoing modification through sulfonation or impregnation of acidic metals.[20] Recent biomass wastes used as sulfonated carbon catalysts were coconut shells,[21] Jatropha hulls,[22] rice husks,[23] empty fruit bunch,[24] corn cobs,[25] etc. Jenie et al. synthesized a mesoporous sulfonated magnetic biochar catalyst to esterify oleic acid optimized at 97.6% (reaction conditions: 5 wt % catalyst loading, 150 °C reaction temperature, 1:8 methanol-to-oil ratio, and 1.5 h reaction time).[26]

In advanced studies, graphite can be converted into graphene oxide (GO) by strong oxidizing agents. Generally, GO is a single carbon sheet that offers a larger surface area for metal oxide nanoparticles to evenly disperse on its surface without agglomeration.[27] GO and r-GO have been used as catalyst supports due to their good adsorption capability, high stability, and high surface area that are useful for photothermal catalysis,[28] dye and contamination adsorption, and catalytic esterification.[29,30] A study reported that the theoretical surface area of GO is 2630 $m^2 g^{-1}$, which would enhance the catalytic lifetime.[31] In addition, GO is rich in oxygen functionality groups such as carboxyl, carbonyl, hydroxy, and epoxy, which can act as catalyst active sites for esterification or provide good oxygenated bonding agreement for sulfonation and metal-GO fabrication.[15,32] Borah et al. synthesized a TiO_2 nanocatalyst supported on reduced GO with average particle sizes of 25−30 nm for the esterification of waste cooking oil.[33] In this study, rGO and ZnO:rGO nanocomposites were synthesized and the evaluation of physical and chemical characteristics was conducted. Then, the catalytic performances of the rGO, ZnO, and ZnO:rGO composites were studied based on their effectiveness in the esterification of acetic acid and *n*-heptanol and the optimized reaction conditions were determined: catalyst screening, reaction temperature, and catalyst loading. The reusability study was carried out using the best performing catalyst.

2. MATERIALS AND METHODS

2.1. Materials. *n*-Dodecane (nDD) (99%), acetic acid (AA) (99.85%), *n*-heptanol (98%), ZnO, and toluene (99.6%) were purchased from Sigma Aldrich (Taufkirchen, Bavaria, Germany).

Methanol (MeOH) (99.5%) and ethanol (EtOH) (96%) were obtained from Fisher Scientific (Loughborough, England, UK). All the chemical reagents were used as available.

2.2. Preparation of GO. GO was synthesized by oxidizing graphite flakes using Hummer's method with modification. Briefly, 1 g of graphite flakes was mixed into concentrated sulfuric acid (25 mL). The mixture was put under continuous stirring, and the resultant mixture was cooled using an ice-water bath to obtain the suspension. Later, under controlled temperature (<10 °C), 3 g of potassium permanganate (KMnO4) as an oxidizing agent was added slowly into the suspension. In the next step, the suspension was then stirred at room temperature for 25 min and then sonicated in an ultrasonic bath for 8−10 min. Distilled water (125 mL) was added into the mixture with 10 times repetition of the stirring−sonication process. Finally, 15 mL of hydrogen peroxide (H2O2) was added into the mixture to exfoliate graphite oxide, which was achieved by ultrasonication of dispersed solution for 1 h. At the end, the final mixture was centrifuged and rGO was washed with 2 M HCl (to remove the excess metal ions) and many times with distilled water (until the pH was neutralized). The obtained rGO precipitates were dried for 24 h at room temperature and labeled as rGO.

2.3. Synthesis of rGO@ZnO Nanocomposites. The prepared 0.04 g of GO nanostructure was dissolved in 100 mL of water for 30 min using ultrasonication, and then 100 mL of aqueous solution of different concentrations of Zn-(CH3COOH)2·2H2O was added slowly with stirring for 15 min. The prepared mixture was then added dropwise to a 1 M hot ethanolic solution of KOH. The final mixture was stirred for 3 h at 100 °C and ultrasonicated for 2 h. Then, the final product was centrifuged and washed with water and methanol several times to remove the impurities. Different concentrations of rGO@ZnO nanocomposites were obtained after drying at 45 °C, and the details of the samples are shown in Table 1.

Table 1. Composition Concentrations of rGO and ZnO

sample code	$Zn(CH_3COOH)_2·2H_2O$ concentration	rGO
$ZnO_{(0.5\ M)}$	0.5 M	no
$ZnO_{(1\ M)}$	1 M	no
$ZnO_{(0.5\ M)}$:rGO	0.5 M	yes
$ZnO_{(1\ M)}$:rGO	1 M	yes
$ZnO_{(1\ M)}$:rGO@300 °C	calcination of S5 at 300 °C, 2 h	
$ZnO_{(1\ M)}$:rGO@500 °C	calcination of S5 at 500 °C, 2 h	

2.4. Catalyst Characterization. The following techniques were used to characterize the rGO and rGO@ZnO nanocomposite catalysts. Thermal degradation was carried out using Shimazdu TGA-50. A Rigaku (Tokyo, Japan) Smart Lab X-ray diffractometer (XRD) with Cu-$K\alpha$ radiation (λ = 1.5406 Å)

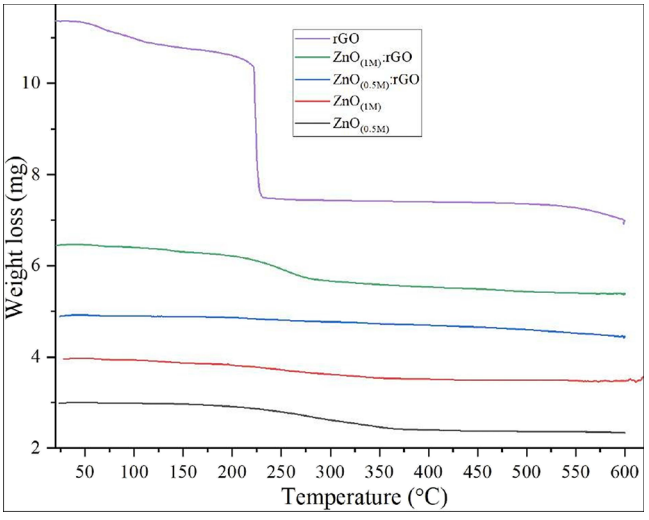

Figure 1. Thermal degradation curves of the uncalcined GO, ZnO, and ZnO:rGO catalysts.

https://doi.org/10.1021/acsomega.1c05565
ACS Omega 2022, 7, 2786−2797

Table 2. Thermal Degradation Analysis

sample	temperature range (°C)	weight loss (wt %)
rGO	25−156	13.10
	156−235	70.13
	235−599	12.05
$ZnO_{(0.5\ M)}$	25−153	1.00
	153−372	13.06
	372−532	1.77
$ZnO_{(1\ M)}$	28−143	4.72
	143−348	18.83
	348−700	6.14
$ZnO_{(0.5\ M)}$:rGO	25−152	0.05
	152−405	2.17
	405−600	3.06
$ZnO_{(1\ M)}$:rGO	21−146	3.24
	146−435	9.25
	435−600	6.97

was used to determine the crystalline nature and to confirm the phase. The Fourier transform infrared spectroscopy (FTIR) measurements were performed in the 4000−400 cm^{-1} range with a KBr pellet method on a Bruker Vertex 70 (Germany) at room temperature. A Quantachrome Nova 2200E-BET (surface area analyzer) was used to determine the pore size distribution and surface area. A JEOL (Tokyo, Japan)-JCM-6000 Plus scanning electron microscope (SEM) and JEOL-JEM-2100 transmission electron microscope (TEM) were utilized to observe the morphological features, particle size, and structural parameters of β-SnWO4 nanoparticles. A JEOL-JED-2200 series energy dispersive X-ray spectrometer (EDX) was utilized for elemental composition determination of the prepared samples at room temperature.

2.5. Catalytic Performance Using Esterification. The catalytic performance of the produced rGO@ZnO nanocomposite catalyst was determined via esterification of AA with *n*-heptanol. The esterification reaction was performed in a 50 mL two-neck round-bottom flask equipped with a reflux condenser and magnetic stirring systems. The said reaction system was immersed in an oil bath, which was assembled with a digitally controlled magnetic stirrer and heater. The reactants, *n*-heptanol and acetic acid with the produced catalyst, rGO@ZnO nanocomposite, were put into the reactor assembly alongside the GC internal standard, nDD. The mixture was stirred at a fixed rate of 400 rpm under atmospheric pressure at a specific temperature for a predefined period of time. The effects on the yield of the reaction of the reaction time (0−160 min), reaction temperature (70−130 °C), and catalyst dose (0.05, 0.10, and 0.15 g) were determined, and the overall results were compared with those obtained for the uncatalyzed reaction.

2.6. Yield Analysis of Esterified AA. A gas chromatogram coupled with a flame ionization detector (GC-FID, Agilent 7890 A, USA) and equipped with a capillary column (BPX-70, 60 m × 0.25 mm × 0.25 μm, Trajan Scientific, AUS) was utilized to determine the quality and yield of the esterified acetic acid profile. Hydrogen gas, as the carrier gas, was employed at a flow rate of 40 mL min^{-1}, and the GC-oven's temperature was set to increase from 100 to 250 °C with a temperature ramp rate of 10 °C min^{-1}. Briefly, 0.5 mL aliquots of the reaction mixtures were carefully collected after every 20 min using a glass syringe, centrifuged, and then injected into the GC-FID. Thus, the area of the chromatograms of esterified acetic acid was calculated via eqs 1−4 to determine the percent yield:

$$K = \frac{\frac{M}{M_o}}{\frac{S}{S_o}} \quad (1)$$

$$X_{AA} = \frac{XM_oS}{S_o} \quad (2)$$

$$Y_{AA} = M - X_{AA} \quad (3)$$

$$C(\%) = \frac{Y_{AA}}{M} \times 100 \quad (4)$$

where M/M_o and S/S_o are the AA/nDD feedstock (by mole) and the peak area ratios, respectively, K is the conversion factor, XAA and YAA are the number of moles of AA unreacted and converted, respectively, and $C(\%)$ is the conversion percentage of AA under the experimental conditions.

3. RESULTS AND DISCUSSION

3.1. Thermal Degradation Analysis. Before catalyst activation through pyrolysis at high temperatures, the thermal degradation of uncalcined samples, rGO, ZnO, and ZnO:rGO, was studied, and the results are presented in Figure 1 and Table 2. The first stage of degradation that occurred at a temperature range of 20−160 °C was attributed to the removal of adsorbed moisture on the catalyst's surface. For the rGO sample, a significant weight loss of 70.13 wt % from 156 to 235 °C was due to the breakdown and loss of labile oxygen functionality groups such as carboxyl, anhydride, or lactone compositions.[28] Meanwhile, a slight weight loss of 12.05 wt % at a temperature beyond 235 °C was attributed to the degradation of stable oxygen components such as phenol, quinone, and carbonyl.[29] Both ZnO samples, $ZnO_{(0.5\ M)}$ and $ZnO_{(1\ M)}$, showed decomposition of acetate ion residue curves at a temperature range of 140−380 °C, with resulting weight losses of 13.06 and 18.83 wt %, respectively.[30] The further thermal degradation that happened up to 700 °C presented that the ZnO samples had achieved stability at high temperatures, as claimed by Kozlowski et al.[31] Upon the co-precipitation between ZnO and rGO ($ZnO_{(0.5\ M)}$:rGO and $ZnO_{(1\ M)}$:rGO), the thermal degradation curves showed significant weight losses of 2.17 and 9.25 wt %, respectively, at a temperature range of 140−450 °C due to the simultaneous degradation of the acetate residue and rGO to form a stable ZnO:rGO compounds.[32] Beyond 450 °C, no major thermal degradation occurred for $ZnO_{(0.5\ M)}$:rGO and $ZnO_{(1\ M)}$:rGO since both catalysts achieved stability.

3.2. X-ray Diffraction. X-ray diffraction patterns of uncalcined ZnO, rGO, and ZnO:rGO samples were measured at diffraction angles of 5−80°, as shown in Figure 2, and the crystalline structures were analyzed and confirmed with the standard card. The diffraction peaks of ZnO were observed at 2θ = 31.76, 34.36, 36.24, 47.56, 56.62, 62.90, 67.04, 68.08, and 69.32° corresponding to the crystal planes (100), (002), (101), (102), (110), (103), (200), (112), and (201), respectively, that matched with JCPDS card no. 36-1451. Meanwhile, the diffraction peaks of rGO were present at 2θ = 11.48 and 42.58° with the crystal planes (001) and (201), respectively, indicating that rGO was successfully synthesized.[59] In addition, the diffraction patterns for ZnO:rGO catalyst samples showed

https://doi.org/10.1021/acsomega.1c05565
ACS Omega 2022, 7, 2786−2797

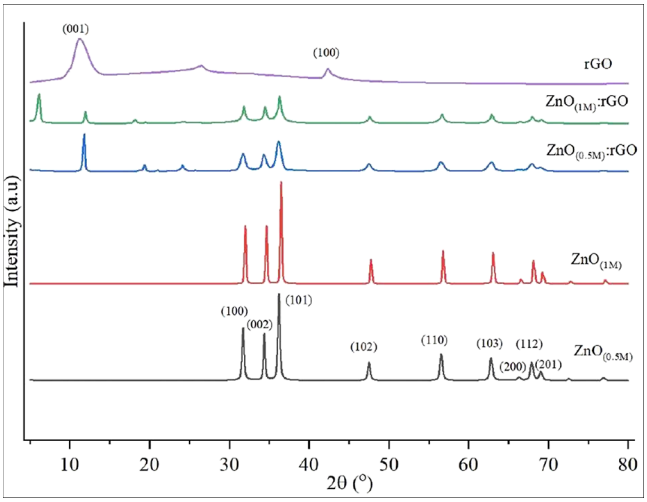

Figure 2. XRD curves of the uncalcined GO, ZnO, and ZnO:rGO catalysts.

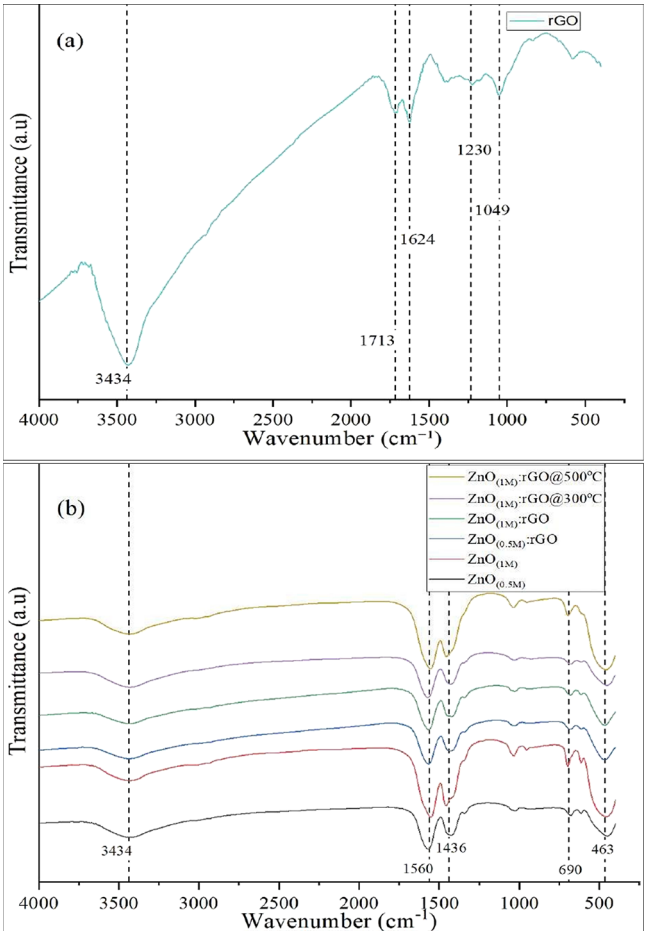

Figure 3. Fourier transform infrared spectroscopy (FT-IR) curves of (a) rGO and (b) ZnO and co-precipitated ZnO:rGO catalysts.

the combination peaks of ZnO and GO.[55] Apart from that, the ZnO peaks of the ZnO:rGO compound showed a lower diffraction intensity in comparison to the pure ZnO due to the dispersion of ZnO on the surface of rGO.[33,50]

3.3. Functional Group Analysis. Figure 3 shows the absorption bands of rGO, ZnO, and the co-precipitated ZnO:rGO catalyst. A typical broad and intense band that was

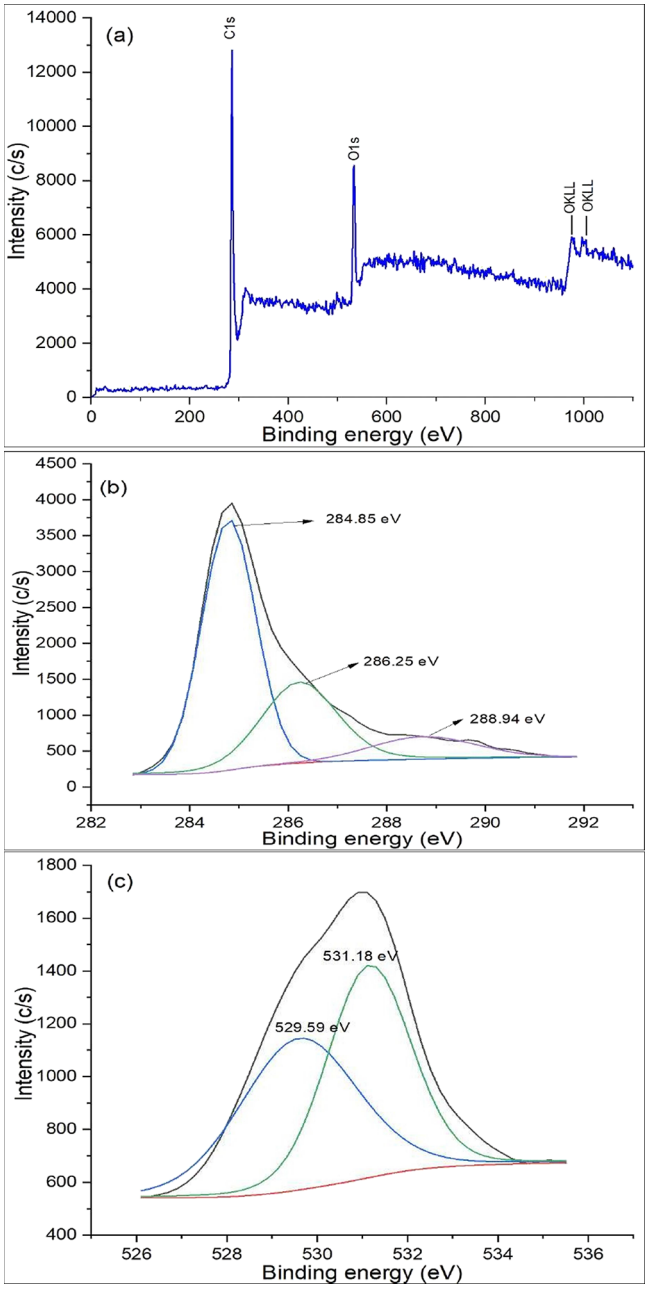

Figure 4. XPS of rGO with a scanning range from 0 to 1200 eV binding energies: (a) wide scan, (b) C 1s scan, and (c) O 1s scan.

attributed to the adsorbed moisture known as the −OH group was found at 3434 cm^{-1}.[34] The IR bands that represent the graphene-oxygen functional groups (Figure 3a) are assigned as follows: 1713 cm^{-1} (C═O, carbonyl and carboxyl stretching), 1230 cm^{-1} (O−C−O, epoxy), and 1049 cm^{-1} (C−O, alkoxy) as well as 1624 cm^{-1} (C═C, aromatic group stretching).[35] The FTIR absorption bands at 1560 and 1436 cm^{-1} of ZnO, ZnO:GO, and calcined Zn:GO are attributed to the asymmetric vibrational band of Zn−O.[36,37] In addition, the spectra at 690 and 463 cm^{-1} represented the stretching vibration between the metal and oxygen (M^{+}−O) of the Zn−O lattice, which proved the formation of a ZnO nanoparticle.[42,43] However, the fabrication of rGO with ZnO caused the FTIR transmittance of ZnO to be markedly reduced.

https://doi.org/10.1021/acsomega.1c05565
ACS Omega 2022, 7, 2786−2797

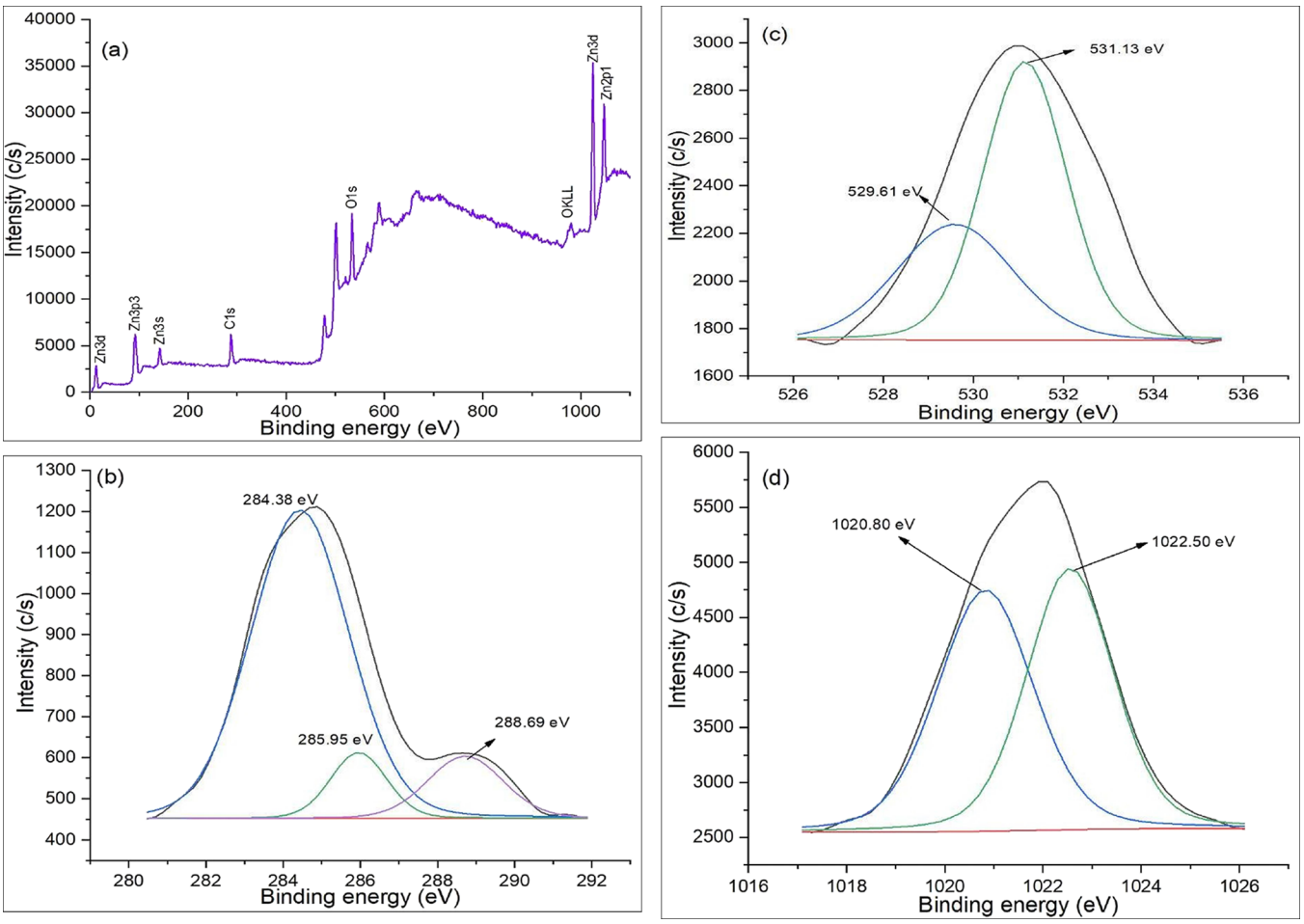

Figure 5. XPS of $ZnO_{(1\ M)}$:GO with a scanning range from 0 to 1200 eV: (a) wide scan, (b) C 1s scan, (c) O 1s scan, and (d) Zn 2p3 scan.

3.4. XPS Analysis. A further advanced investigation of the surface chemical properties of representative catalysts, rGO and $ZnO_{(1\ M)}$:rGO, was carried out by X-ray photoelectron spectroscopy as shown in Figures 4 and 5, respectively. The peaks observed at 284.55, 286.25, and 288.94 eV in the C 1s spectrum of rGO (Figure 4b) were attributed to the non-oxygenated bonding of C−C/C═C, C−OC of epoxyl/alkoxyl groups, and carbonyl group, C═O, respectively.[31,44] As the reduced graphene oxide is made up of carbon−oxygen components, the O 1s bands (Figure 4c) were detected at 529.59 and 531.18 eV, which correspond to the C═O/O═C−OH and C−OH (hydroxyl) functional groups, respectively.[10,45] The combination of ZnO and GO ($ZnO_{(1\ M)}$:rGO) reproduced likely the same binding band energies of C 1s (Figure 5b) at 284.38, 285.95, and 288.69 eV due to carbon−oxygen rich groups as discussed in the previous paragraph.[58,60] Meanwhile, the O 1s signal of $ZnO_{(1\ M)}$:GO in Figure 5c reveals the formation of metal oxide and metal carbonate functional groups at 529.61 and 531.13 eV, respectively.[46,47] The ZnO bands were present at 1020.80 and 1022.59 eV, in which both signals were attributed to the tetrahedrally (loss two oxygen atom bonds) and hexagonally coordinated ZnO crystals, respectively.[48]

3.5. Textural Surface Properties. The textural properties of the rGO, ZnO, and Zn:rGO nanoparticle samples such as the surface area, pore diameter, and pore volume were evaluated using a Micrometrics ASAP-2020 under liquid nitrogen cryogenic temperature. As shown in Figure 6a, the synthesized nanomaterials exhibited a type-IV mesoporous nitrogen adsorption−desorption behavior with the H-2 hysteresis loops (ink-bottle shape pore) owing to rGO while the rest of the samples displayed the H-3 hysteresis loop (slit-like pore), as per IUPAC classification.[38] The pore distribution corresponding to the sample's BET absorption−desorption was calculated using the BJH formula, as shown in Figure 6b. The samples consisted of a broad and multi hierarchically organized mesoporous structure with maximum peak pore diameters from 2 to 50 nm, which are tabulated in Table 3. The result showed that the small mesopores indicate that pores exist within nanosheets while large mesopores were fabricated between stacked nanosheets.[39] The surface areas of rGO, $ZnO_{(0.5\ M)}$, and $ZnO_{(1\ M)}$ were recorded, respectively, at 31.72, 27.65, and 36.19 $m^2\ g^{-1}$, respectively. A considerable decrease in surface areas was observed after rGO and ZnO (0.5 and 1.0 M) were co-precipitated and calcined at 300 and 500 °C. This indicated that the surface areas of both components were occupied by each other while the calcination process influenced the increase in the pore size by reducing the surface area.[40]

3.6. Microscopy Morphology of Synthesized Catalysts. The microscopy images of the synthesized rGO, ZnO, ZnO:rGO, and calcined ZnO:rGO were observed at 30K magnification, as presented in Figure 7. Figure 7a shows the layered planar structure with a wrinkled surface of rGO, which is in agreement with a previous study by Xi et al.[44] The micrograph in Figure 7b,c revealed the hexagonal structure of

https://doi.org/10.1021/acsomega.1c05565
ACS Omega 2022, 7, 2786−2797

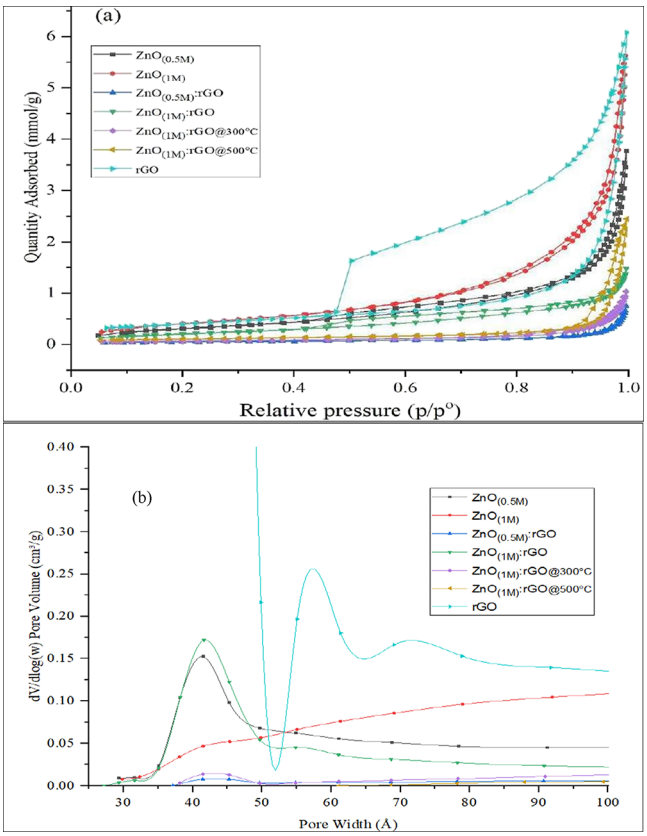

Figure 6. (a) Nitrogen adsorption/desorption isotherms of the rGO and ZnO and ZnO:rGO nanocomposite catalysts. (b) Pore volume curves of the rGO and ZnO and co-precipitated ZnO:rGO catalysts.

Table 3. BET Surface Areas, Pore Diameters, and Pore Volumes of the Prepared rGO and Composite ZnO:rGO

catalyst	surface area ($m^2\ g^{-1}$)	pore diameter (nm)	pore volume ($cm\ g^{-1}$)
rGO	31.72	7.80	0.27
$ZnO_{(0.5\ M)}$	27.65	14.43	0.13
$ZnO_{(1\ M)}$	36.19	18.95	0.20
$Zn_{(0.5\ M)}$:rGO	17.49	10.73	0.05
$Zn_{(1\ M)}$:rGO	18.52	8.11	0.05
$Zn_{(1\ M)}$:rGO@300 °C	5.63	24.88	0.04
$Zn_{(1\ M)}$:rGO@500 °C	8.63	42.65	0.08

Table 4. Elemental Composition of rGO, ZnO, and ZnO:rGO Composites

	element (mass %)		
sample	C	O	Zn
$ZnO_{(0.5\ M)}$		44.43	55.57
$ZnO_{(1\ M)}$		24.53	75.47
$ZnO_{(0.5\ M)}$:rGO	43.46	13.09	43.45
$ZnO_{(1\ M)}$:rGO	29.54	14.45	56.00

the synthesized $ZnO_{(0.5\ M)}$ and $ZnO_{(1\ M)}$ nanoparticles, respectively. These particles were bound together by stacking to each other.[51] Surface modification was performed after the preparation of the ZnO:rGO nanomaterial, as shown in Figure 7d,e, for comparison with their parent morphology structures. It is observed that various sizes of ZnO nanoparticles were dispersed and deposited on rGO surface sheets through Zn−O−C bonding during pyrolysis, as shown in Figure 7f,g.

3.7. Transmission Electron Microscopy Analysis. Further insights into the morphology of ZnO and ZnO:rGO were examined by transmission electron microscopy under 500K magnification power, as shown in Figure 8. Figure 8a clearly shows the hexagonally coordinated ZnO structure with orderly arrangement, which is in agreement with the SEM images. Meanwhile, in Figure 8b, ZnO was well distributed on the surface of GO with two different crystal orientations, tetrahedral and hexagonal Zn atoms, as discussed in Section 3.4.

3.8. Elemental Analysis by Energy Dispersive X-ray Spectroscopy. The elemental compositions (mass %) for the synthesized ZnO and ZnO:rGO were measured by a JOEL-JED:2200 series spectrometer, as shown in the measurements in Table 4 and Figure 9. The results show that the elemental mass percent of Zn increased proportionally with its molar concentration for both the monocomponent (0.5 and 1 M) and the ZnO:rGO composite nanoparticles. In addition, this analysis proved that the ZnO:rGO nanocomposites were successfully synthesized due to the presence of Zn, O, and C, which was also in agreement with XRD and FTIR. The carbon composition of $ZnO_{(1\ M)}$:rGO was slightly lower due to the higher distribution of ZnO on the surface of rGO, which is clearly shown in the textural surface property analyses as well as microscopy analyses using SEM.

3.9. Catalytic Performance Studies. The catalytic esterification of acetic acid and *n*-heptanol was tested using the synthesized rGO, ZnO, and ZnO:rGO catalysts in the reflux system, which was equipped with a cold condenser. The esterification parameters such as the reaction time (0−160 min of 20 min interval), catalyst loading (0.05, 0.10, and 0.15 g), and reaction temperature (70−130 °C of 20 °C interval) were studied to achieve the optimum biodiesel conversion, as shown in Figure 10. The amount of heptanol was fixed at 9.06 g.

Figure 10a shows the comparison of the conversion percentages of biodiesel without a catalyst and in the presence of the prepared catalyst at a constant reaction temperature of 110 °C and catalyst loading of 0.10 g. The conversion percentage increased with increasing reaction time regardless of the type of catalyst utilized in the reaction. According to the reported result, conversion yields differed considerably to the catalytic performances of the tested catalysts. In this experiment, the uncatalyzed acetic acid with heptanol reaction was slow and only converted 24.02% of biodiesel after 160 min. Meanwhile, the biodiesel conversion was improved upon catalytic esterification due to the presence of catalysts that enhance the heptanol solubility by increasing the reaction rate with acetic acid for conversion of ester within a shorter reaction time.[52] Generally, catalysts would speed up the reaction rate; however, the chemical and physical characteristics of the catalyst itself could affect the reaction mixture, favoring either a forward or backward reaction.[53,54] Among the tested catalysts, the rGO sample catalyzed the highest biodiesel conversion of 100% for three consecutive reaction times (120, 140, and 160 min) while the other samples barely achieved a catalytic conversion more than 75% with the same reaction time. Generally, the rGO sample consisted of a higher number of oxygen functional groups that acted as active sites, which enhanced the catalytic performance in comparison with the other prepared catalysts.[41] In addition, the rGO catalyst had a large surface area and narrow pore diameter that enhanced and facilitated the diffusion of acetic acid and heptanol effectively toward the available active sites.[42] Thus, the rGO catalyst was

https://doi.org/10.1021/acsomega.1c05565
ACS Omega 2022, 7, 2786−2797

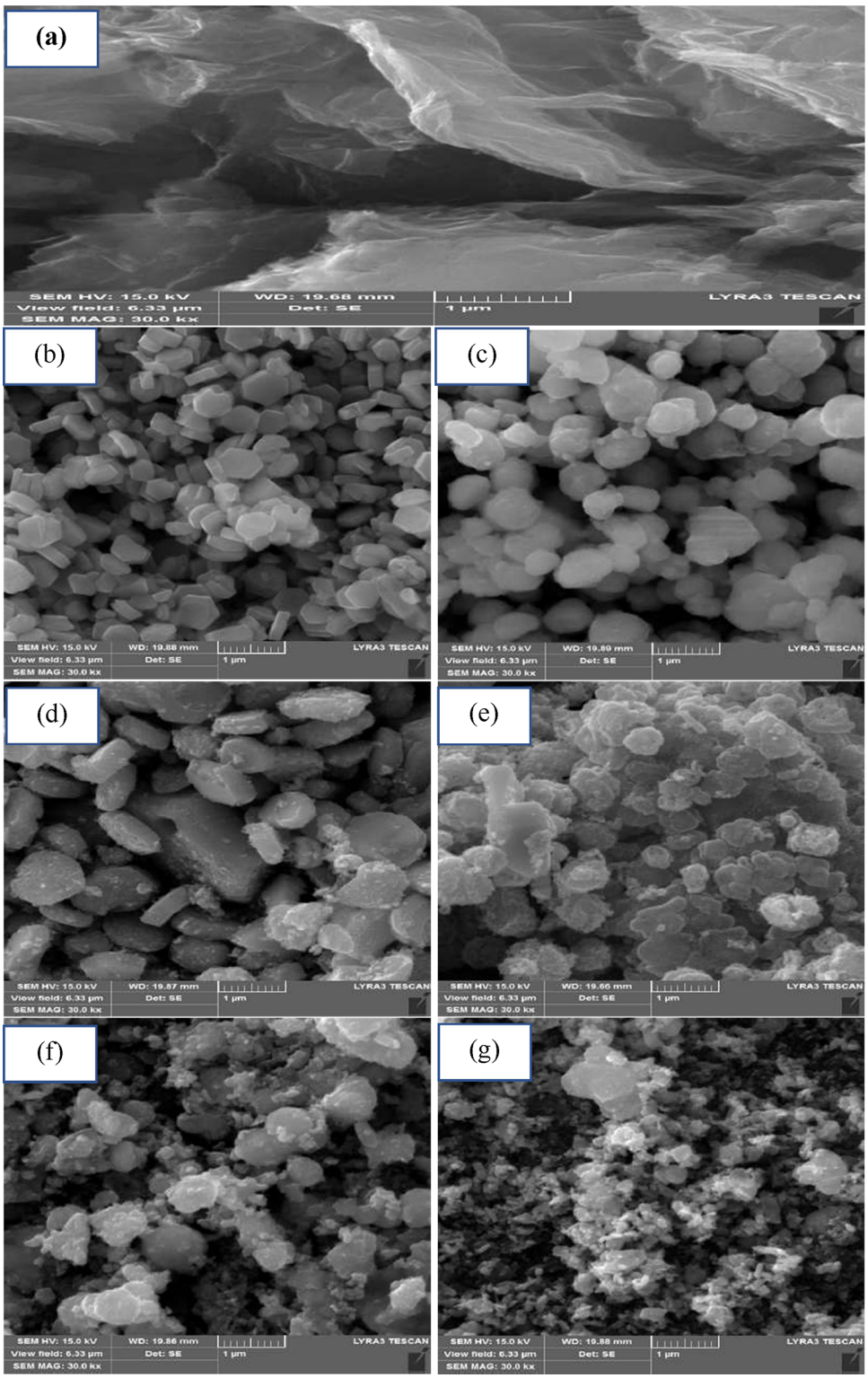

Figure 7. SEM images at 30K magnification: (a)rGO, (b) $ZnO_{(0.5\ M)}$, (c) $ZnO_{(1\ M)}$, (d) $ZnO_{(0.5\ M)}$:rGO, (e) $ZnO_{(1\ M)}$:rGO, (f) $ZnO_{(1\ M)}$:rGO@300 °C, and (g) $ZnO_{(1\ M)}$:rGO@500 °C.

designated for further optimization reactions. Meanwhile, the reaction rates for the esterification of acetic acid by using the ZnO (0.5 M and 1.0 M) nanocatalyst and Zn:rGO composites was less favorable due to the ZnO basicity characteristic[56,61] that complicates the conversion process in comparison with rGO. In addition, upon the fabrication of the composite catalyst, the Zn ions contributed in reducing the Bronsted base availability of the negatively charged ions of oxygen from rGO, thus reducing the catalytic performance of ZnO:rGO.[57]

Catalytic esterification performance investigation on the effect of the catalyst loading toward the conversion of biodiesel at a constant reaction temperature, 110 °C, was conducted. As illustrated in Figure 10b, the conversion rate increased proportionally with the catalyst loading and reaction time. A

https://doi.org/10.1021/acsomega.1c05565
ACS Omega 2022, 7, 2786−2797

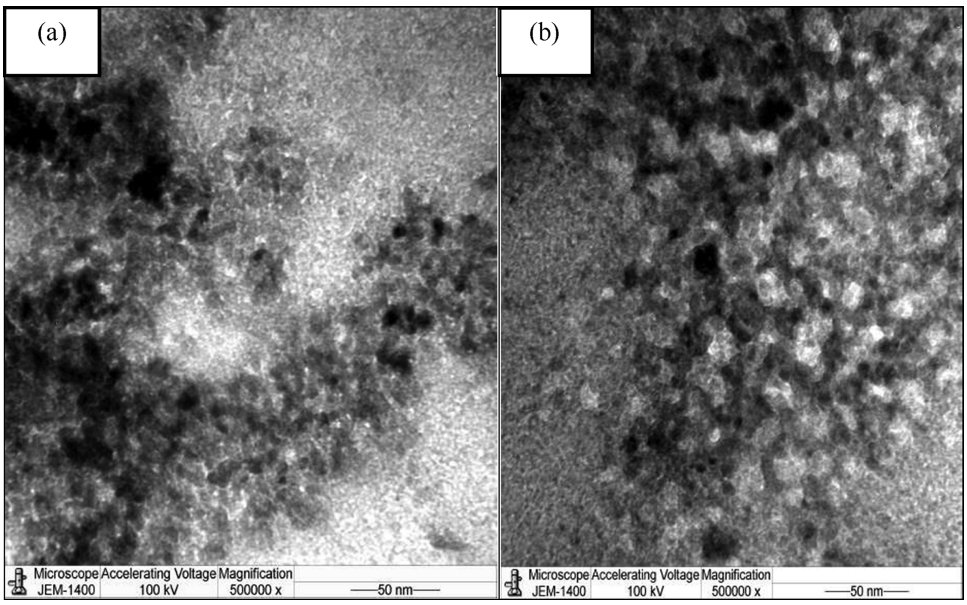

Figure 8. TEM image of (a) $ZnO_{(1\ M)}$ and (b) $ZnO_{(1\ M)}$:rGO.

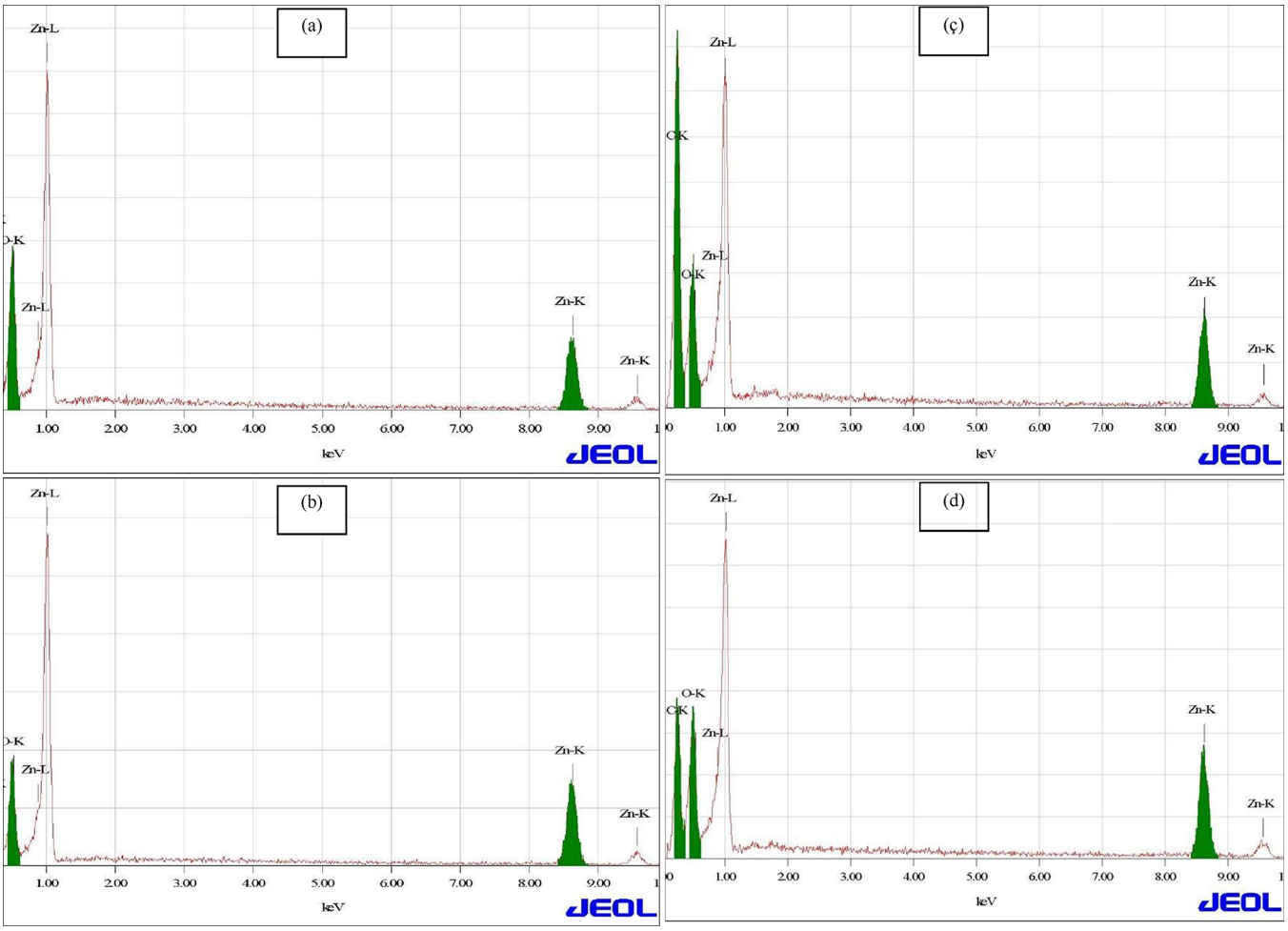

Figure 9. Elemental analysis using an EDX spectrometer: (a) $ZnO_{(0.5\ M)}$, (b) $ZnO_{(1\ M)}$, (c) $ZnO_{(0.5\ M)}$:rGO, and (d) $ZnO_{(1\ M)}$:rGO.

catalyst loading of 0.05 g of rGO converted the acetate ester at a longer reaction time of 140 min to achieve 100%, while the conversion using 0.10 and 0.15 g of rGO occurred after 120 and 80 min, respectively. At a lower catalyst loading, the reactants would compete to diffuse on the active sites, and thus it took a longer time for the conversion to complete.[43] Nevertheless, there was no further result of esterification with 0.15 g of catalyst beyond 100 min due to solidification of

https://doi.org/10.1021/acsomega.1c05565
ACS Omega 2022, 7, 2786−2797

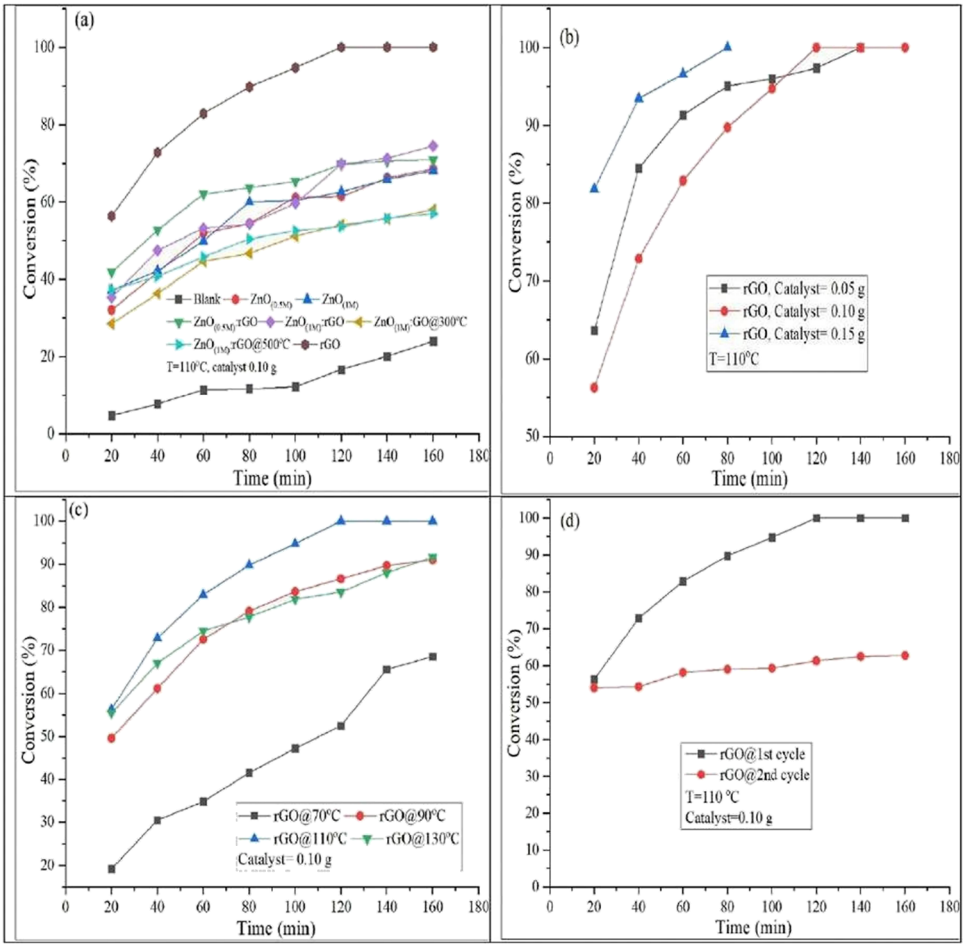

Figure 10. Catalytic esterification of acetic acid at reaction times from 0 to 160 min with a constant amount of 9.06 g of heptanol. (a) Catalyst screening (with a fixed catalyst loading = 0.10 g, reaction temperature = 110 °C). (b) Catalyst loading (at a constant reaction temperature = 110 °C). (c) Reaction temperature (with a fixed catalyst loading = 0.10 g). (d) Catalyst reusability (with a fixed catalyst loading = 0.10 g, reaction temperature = 110 °C).

reactants that occurred as a result of mass transfer limitation between reactants and the catalyst.[44] The optimum catalyst loading was identified to be 0.10 g, obtaining 100% yield constantly for three consecutive runs with a 20 min interval (120, 140, and 160 min).

Referring to Figure 10c, the conversion increased with the increase in temperature, in which 100% of conversion was obtained at 110 °C. As the temperature increased, the esterification reaction would speed up due to the increase in reactants' vibrational kinetic energy (effective collision) that enhanced the reaction rate, which led to the miscibility of acetic acid and heptanol on the surface of active sites.[45] However, the conversion reduced as the temperature exceeded 110 °C due to the evaporation of *n*-heptanol, and thus, the availability of the alcohol decreased.[46]

The catalyst reusability of rGO was studied for at least two catalytic cycles, as shown in Figure 10d to investigate the effectiveness of the catalytic performance after multiple uses under optimized reaction parameters. The obtained conversion of the second catalytic cycle was 62.79%, which was nearly 40% reduction from the first cycle at 160 min due to the deactivation of the catalyst. This phenomenon might occur as a result of agglomeration of the remaining reactants or intermediate products on the active site surface, reducing the number of active sites as well as inhibiting the esterification reaction.[47,49] In addition, the changes in the physical and chemical properties of the catalyst contributed to the loss of catalytic activities, which requires further investigation in the future.

4. CONCLUSIONS

This research reports the successful synthesis of rGO-metal oxide composite catalysts through a modification method for the esterification of acetic acid (AA) with *n*-heptanol. It was found that the metal oxide rGO-based composite showed better properties than rGO in terms of textural properties, which is important in improving the esterification reaction. The structural properties of GO and GO-metal oxide composite catalysts, determined by FTIR, TGA, BET, SEM, TEM, and EDX, showed that they are effective catalysts for the esterification of AA. The ZnO-rGO-based composite catalysts were used for the esterification of AA, which gave a high conversion of 100% with optimal reaction conditions of 0.1 wt % catalyst, 160 min reaction time, and 170 °C reaction temperature. The reusability study revealed that the catalyst is stable for two reaction cycles; further study on regeneration should be performed. The produced catalysts showed potential for esterification reaction conversion; in this regard, it can be used for other conversions such as biodiesel production.

https://doi.org/10.1021/acsomega.1c05565
ACS Omega 2022, 7, 2786−2797

AUTHOR INFORMATION

Corresponding Author

Fahad A. Alharthi − *College of Science, Department of Chemistry, King Saud University, Riyadh 11451, Saudi Arabia;* orcid.org/0000-0001-7513-9777; Email: fharthi@ksu.edu.sa

Authors

Amjad Abdullah Alsyahi − *College of Science, Department of Chemistry, King Saud University, Riyadh 11451, Saudi Arabia*

Saad G. Alshammari − *College of Science, Department of Chemistry, King Saud University, Riyadh 11451, Saudi Arabia*

Hessah A. AL-Abdulkarim − *College of Science, Department of Chemistry, King Saud University, Riyadh 11451, Saudi Arabia*

Amal AlFawaz − *College of Science, Department of Chemistry, King Saud University, Riyadh 11451, Saudi Arabia*

Ali Alsalme − *College of Science, Department of Chemistry, King Saud University, Riyadh 11451, Saudi Arabia;* orcid.org/0000-0003-0897-2296

Complete contact information is available at: https://pubs.acs.org/10.1021/acsomega.1c05565

Author Contributions

†F.A.A. and H.A.A. contributed equally to this work.

Notes

The authors declare no competing financial interest.

ACKNOWLEDGMENTS

The authors extend thanks to the Researchers Supporting Project (Ref: RSP-2021/160), King Saud University (Riyadh, Saudi Arabia).

LIST OF ABBREVIATIONS

BET	Brunauer−Emmett−Teller
SEM	scanning electron microscope
TEM	transmission electron microscope
XRD	X-ray diffraction spectroscopy
XPS	X-ray photoelectron spectroscopy
TGA	thermogravimetric analysis
FTIR	Fourier transform infrared spectroscopy
EDX	energy dispersive X-ray analysis
ICP	inductively coupled plasma analysis
rGO	reduced graphene oxide
FFA	free fatty acid
AA	acetic acid
ZnO	zinc oxide

REFERENCES

(1) Loy, A. C. M.; Quitain, A. T.; Lam, M. K.; Yusup, S.; Sasaki, M.; Kida, T. Development of high microwave-absorptive bifunctional graphene oxide-based catalyst for biodiesel production. *Energy Convers. Manage.* **2019**, *180*, 1013−1025.

(2) AbuKhadra, M. R.; Basyouny, M. G.; El-Sherbeeny, A. M.; El-Meligy, M. A.; Abd Elgawad, A. E. E. Transesterification of commercial waste cooking oil into biodiesel over innovative alkali trapped zeolite nanocomposite as green and environmental catalysts. *Sustain. Chem. Pharm.* **2020**, *17*, 100289.

(3) Sangaletti-Gerhard, N.; Cea, M.; Risco, V.; Navia, R. In situ biodiesel production from greasy sewage sludge using acid and enzymatic catalysts. *Bioresour. Technol.* **2015**, *179*, 63−70.

(4) Nisar, J.; Razaq, R.; Farooq, M.; Iqbal, M.; Khan, R. A.; Sayed, M.; Shah, A.; ur Rahman, I. Enhanced biodiesel production from Jatropha oil using calcined waste animal bones as catalyst. *Renewable Energy* **2017**, *101*, 111−119.

(5) Syazwani, O. N.; Rashid, U.; Mastuli, M. S.; Taufiq-Yap, Y. H. Esterification of palm fatty acid distillate (PFAD) to biodiesel using Bi-functional catalyst synthesized from waste angel wing shell (Cyrtopleura costata). *Renewable Energy* **2019**, *131*, 187−196.

(6) Amabat, I.; Srivastava, V.; Iftekhar, S.; Haapaniemi, E.; Sillanpää, M. Effect of different co-solvents on biodiesel production from various low-cost feedstocks using Sr−Al double oxides. *Renewable Energy* **2020**, *146*, 2158−2169.

(7) Toldrá-Reig, F.; Mora, L.; Toldrá, F. Developments in the use of lipase transesterification for biodiesel production from animal fat waste. *Appl. Sci.* **2020**, *10*, 5085.

(8) Abdullah, S. H. Y. S.; Hanapi, N. H. M.; Azid, A.; Umar, R.; Juahir, H.; Khatoon, H.; Endut, A. A review of biomass-derived heterogeneous catalyst for a sustainable biodiesel production. *Renewable Sustainable Energy Rev.* **2017**, *70*, 1040−1051.

(9) Sree, J. V.; Chowdary, B. A.; Kumar, K. S.; Anbazhagan, M. P.; Subramanian, S. Optimization of the biodiesel production from waste cooking oil using homogeneous catalyst and heterogeneous catalysts. *Mater. Today: Proc.* **2021**, *46*, 4900−4908.

(10) Zhang, N.; Qiu, Y.; Sun, H.; Hao, J.; Chen, J.; Xi, J.; Liu, J.; He, B.; Bai, Z. W. Substrate- Assisted Encapsulation of Pd-Fe Bimetal Nanoparticles on Functionalized Silica Nanotubes for Catalytic Hydrogenation of Nitroarenes and Azo Dyes. *ACS Appl. Nano Mater.* **2021**, *4*, 5854−5863.

(11) Eze, V. C.; Phan, A. N.; Harvey, A. P. Intensified one-step biodiesel production from high water and free fatty acid waste cooking oils. *Fuel* **2018**, *220*, 567−574.

(12) Soltani, S.; Rashid, U.; Yunus, R.; Taufiq-Yap, Y. H. Biodiesel production in the presence of sulfonated mesoporous ZnAl2O4 catalyst via esterification of palm fatty acid distillate (PFAD). *Fuel* **2016**, *178*, 253−262.

(13) Saba, T.; Estephane, J.; El Khoury, B.; El Khoury, M.; Khazma, M.; El Zakhem, H.; Aouad, S. Biodiesel production from refined sunflower vegetable oil over KOH/ZSM5 catalysts. *Renewable Energy* **2016**, *90*, 301−306.

(14) Ngaosuwan, K.; Lotero, E.; Suwannakarn, K.; Goodwin, J. G., Jr.; Praserthdam, P. Hydrolysis of triglycerides using solid acid catalysts. *Ind. Eng. Chem. Res.* **2009**, *48*, 4757−4767.

(15) Wang, D.; Liu, J.; Xi, J.; Jiang, J.; Bai, Z. Pd-Fe dual-metal nanoparticles confined in the interface of carbon nanotubes/N-doped carbon for excellent catalytic performance. *Appl. Surf. Sci.* **2019**, *489*, 477−484.

(16) Xi, J.; Wang, Q.; Duan, X.; Zhang, N.; Yu, J.; Sun, H.; Wang, S. Continuous flow reduction of organic dyes over Pd-Fe alloy based fibrous catalyst in a fixed-bed system. *Chem. Eng. Sci.* **2021**, *231*, 116303.

(17) Vargas, E. M.; Neves, M. C.; Tarelho, L. A. C.; Nunes, M. I. Solid catalysts obtained from wastes for FAME production using mixtures of refined palm oil and waste cooking oils. *Renewable Energy* **2019**, *136*, 873−883.

(18) Wei, Y.; Shen, C.; Xie, J.; Bu, Q. Study on reaction mechanism of superior bamboo biochar catalyst production by molten alkali carbonates pyrolysis and its application for cellulose hydrolysis. *Sci. Total Environ.* **2020**, *712*, 136435.

(19) Liu, K.; Wang, R.; Yu, M. An efficient, recoverable solid base catalyst of magnetic bamboo charcoal: Preparation, characterization, and performance in biodiesel production. *Renewable Energy* **2018**, *127*, 531−538.

(20) Sun, X.; Atiyeh, H. K.; Li, M.; Chen, Y. Biochar facilitated bioprocessing and biorefinery for productions of biofuel and chemicals: A review. *Bioresour. Technol.* **2020**, *295*, 122252.

(21) Hidayat, A.; Rochmadi; Wijaya, K.; Nurdiawati, A.; Kurniawan, W.; Hinode, H.; Yoshikawa, K.; Budiman, A. Esterification of Palm Fatty Acid Distillate with High Amount of Free Fatty Acids Using Coconut Shell Char Based Catalyst. *Energy Proc.* **2015**, *75*, 969−974.

(22) Zhang, F.; Tian, X.; Shah, M.; Yang, W. Synthesis of magnetic carbonaceous acids derived from hydrolysates of Jatropha hulls for catalytic biodiesel production. *RSC Adv.* **2017**, *7*, 11403−11413.
(23) Guo, M. L.; Yin, X. Y.; Huang, J. Preparation of novel carbonaceous solid acids from rice husk and phenol. *Mater. Lett.* **2017**, *196*, 23−25.
(24) Ravi, A.; Gurunathan, B.; Rajendiran, N.; Varjani, S.; Gnansounou, E.; Pandey, A.; You, S.; Raman, J. K.; Ramanujam, P. Contemporary approaches towards augmentation of distinctive heterogeneous catalyst for sustainable biodiesel production. *Environ. Technol. Innov.* **2020**, *19*, 100906.
(25) Ibrahim, S. F.; Asikin-Mijan, N.; Ibrahim, M. L.; Abdulkareem-Alsultan, G.; Izham, S. M.; Taufiq-Yap, Y. H. Sulfonated functionalization of carbon derived corncob residue via hydrothermal synthesis route for esterification of palm fatty acid distillate. *Energy Convers. Manage.* **2020**, *210*, 112698.
(26) Jenie, S.N.A.; Kristiani, A.; Sudiyarmanto; Khaerudini, D.S.; Takeishi, K.; Khaerudini, D.S.; Takeishi, K. Sulfonated magnetic nanobiochar as heterogeneous acid catalyst for esterification reaction. *J. Environ. Chem. Eng.* **2020**, *8*, 103912.
(27) Soltani, S.; Khanian, N.; Shean Yaw Choong, T.; Asim, N.; Zhao, Y. Microwave- assisted hydrothermal synthesis of sulfonated TiO2-GO core−shell solid spheres as heterogeneous esterification mesoporous catalyst for biodiesel production. *Energy Convers. Manage.* **2021**, *238*, 114165.
(28) Xi, J.; Huang, J.; Wang, D.; Wen, L.; Hao, J.; He, B.; Chen, J.; Bai, Z. W. Probing Activity Enhancement of Photothermal Catalyst under Near-Infrared Irradiation. *J. Phys. Chem. Lett.* **2021**, *12*, 3443−3448.
(29) Jo, J.; Yoon, J.; Lee, T.; Cho, H. Y.; Lee, J. Y.; Choi, J. W. H2O2 biosensor consisted of hemoglobin-DNA conjugate on nanoporous gold thin film electrode with electrochemical signal enhancement. *Nano Converg.* **2019**, *6*, 1−8.
(30) Yek, S. M. G.; Azarifar, D.; Nasrollahzadeh, M.; Bagherzadeh, M.; Shokouhimehr, M. Heterogenized Cu(II) complex of 5-aminotetrazole immobilized on graphene oxide nanosheets as an efficient catalyst for treating environmental contaminants. *Sep. Purif. Technol.* **2020**, *247*, 116952.
(31) Gaidukevic, J.; Barkauskas, J.; Malaika, A.; Rechnia-Goracy, P.; Mozdzyńska, A.; Jasulaitiene, V.; Kozlowski, M. Modified graphene-based materials as effective catalysts for transesterification of rapeseed oil to biodiesel fuel. *Chin. J. Catal.* **2018**, *39*, 1633−1645.
(32) Roy, A. S.; Cheruvathoor Poulose, A.; Bakandritsos, A.; Varma, R. S.; Otyepka, M. 2D graphene derivatives as heterogeneous catalysts to produce biofuels via esterification and trans-esterification reactions. *Appl. Mater. Today* **2021**, *23*, 101053.
(33) Borah, M. J.; Devi, A.; Saikia, R. A.; Deka, D. Biodiesel production from waste cooking oil catalyzed by in-situ decorated TiO2 on reduced graphene oxide nanocomposite. *Energy* **2018**, *158*, 881−889.
(34) dos Santos, T. C.; Santos, E. C. S.; Dias, J. P.; Barreto, J.; Stavale, F. L.; Ronconi, C. M. Reduced graphene oxide as an excellent platform to produce a stable BrØnsted acid catalyst for biodiesel production. *Fuel* **2019**, *256*, 115793.
(35) Bai, L.; Tajikfar, A.; Tamjidi, S.; Foroutan, R.; Esmaeili, H. Synthesis of MnFe2O4@graphene oxide catalyst for biodiesel production from waste edible oil. *Renewable Energy* **2021**, *170*, 426−437.
(36) Hu, C.; Mi, J.; Shang, S.; Shangguan, J. The study of thermal decomposition kinetics of zinc oxide formation from zinc oxalate dihydrate. *J. Therm. Anal. Calorim.* **2014**, *115*, 1119−1125.
(37) Borah, M. J.; Devi, A.; Borah, R.; Deka, D. Synthesis and application of Co doped ZnO as heterogeneous nanocatalyst for biodiesel production from non-edible oil. *Renewable Energy* **2019**, *133*, 512−519.
(38) Pradhan, G.; Sharma, Y. C. Green synthesis of glycerol carbonate by transesterification of bio glycerol with dimethyl carbonate over Mg/ZnO: A highly efficient heterogeneous catalyst. *Fuel* **2021**, *284*, 118966.
(39) Hazmi, B.; Rashid, U.; Taufiq-yap, Y. H.; Ibrahim, M. L. Supermagnetic Nano- Bifunctional Catalyst from Rice Husk: Synthesis, Characterization and Application for Conversion of Used Cooking Oil to Biodiesel. *Catalysts* **2020**, 225.
(40) Masteri-Farahani, M.; Hosseini, M. S.; Forouzeshfar, N. Propyl-SO3H functionalized graphene oxide as multipurpose solid acid catalyst for biodiesel synthesis and acid- catalyzed esterification and acetalization reactions. *Renewable Energy* **2020**, *151*, 1092−1101.
(41) Hassan, H. M. A.; Alhumaimess, M. S.; Alsohaimi, I. H.; Essawy, A. A.; Hussein, M. F.; Alshammari, H. M.; Aldosari, O. F. Biogenic-mediated synthesis of the Cs2O- MgO/MPC nano-composite for biodiesel production from olive oil. *ACS Omega* **2020**, *5*, 27811−27822.
(42) Ashok, A.; Kennedy, L. J.; Vijaya, J. J. Structural, optical and magnetic properties of Zn1-xMnxFe2O4 ($0 \leq x \leq 0.5$) spinel nano particles for transesterification of used cooking oil. *J. Alloys Compd.* **2019**, *780*, 816−828.
(43) Haghighatzadeh, A.; Mazinani, B.; Ostad, M.; Shokouhimehr, M.; Dutta, J. Hollow ZnO microspheres self-assembled from rod-like nanostructures: morphology-dependent linear and Kerr-type non-linear optical properties. *J. Mater. Sci.: Mater. Electron.* **2021**, *32*, 23385−23398.
(44) Xi, J.; Sun, H.; Wang, D.; Zhang, Z.; Duan, X.; Xiao, J.; Xiao, F.; Liu, L.; Wang, S. Confined-interface-directed synthesis of Palladium single-atom catalysts on graphene/amorphous carbon. *Appl. Catal. B Environ.* **2018**, *225*, 291−297.
(45) Torrisi, L.; Silipigni, L.; Cutroneo, M.; Torrisi, A. Graphene oxide as a radiation sensitive material for XPS dosimetry. *Vacuum* **2020**, *173*, 109175.
(46) Laskar, I. B.; Deshmukhya, T.; Bhanja, P.; Paul, B.; Gupta, R.; Chatterjee, S. Transesterification of soybean oil at room temperature using biowaste as catalyst; an experimental investigation on the effect of co-solvent on biodiesel yield. *Renewable Energy* **2020**, *162*, 98−111.
(47) Gohain, M.; Laskar, K.; Phukon, H.; Bora, U.; Kalita, D.; Deka, D. Towards sustainable biodiesel and chemical production: Multi-functional use of heterogeneous catalyst from littered Tectona grandis leaves. *Waste Manage.* **2020**, *102*, 212−221.
(48) Bhowmick, T. K.; Suresh, A. K.; Kane, S. G.; Joshi, A. C.; Bellare, J. R. Physicochemical characterization of an Indian traditional medicine, Jasada Bhasma: Detection of nanoparticles containing non-stoichiometric zinc oxide. *J. Nanopart. Res.* **2009**, *11*, 655−664.
(49) Dhawane, S. H.; Kumar, T.; Halder, G. Recent advancement and prospective of heterogeneous carbonaceous catalysts in chemical and enzymatic transformation of biodiesel. *Energy Convers. Manage.* **2018**, *167*, 176−202.
(50) Deng, J.; Li, M.; Wang, Y. Biomass-derived carbon: Synthesis and applications in energy storage and conversion. *Green Chem.* **2016**, *18*, 4824−4854.
(51) Alsharifi, M.; Znad, H.; Hena, S.; Ang, M. Biodiesel production from canola oil using novel Li/TiO2 as a heterogeneous catalyst prepared via impregnation method. *Renewable Energy* **2017**, *114*, 1077−1089.
(52) Awogbemi, O.; Von Kallon, D. V.; Aigbodion, V. S. Trends in the development and utilization of agricultural wastes as heterogeneous catalyst for biodiesel production. *J. Energy Inst.* **2021**, *98*, 244−258.
(53) Chua, S. Y.; Periasamy, L. A.; Goh, C. M. H.; Tan, Y. H.; Mubarak, N. M.; Kansedo, J.; Khalid, M.; Walvekar, R.; Abdullah, E. C. Biodiesel synthesis using natural solid catalyst derived from biomass waste — A review. *J. Ind. Eng. Chem.* **2020**, *81*, 41−60.
(54) Cheng, J.; Qiu, Y.; Huang, R.; Yang, W.; Zhou, J.; Cen, K. Biodiesel production from wet microalgae by using graphene oxide as solid acid catalyst. *Bioresour. Technol.* **2016**, *221*, 344−349.
(55) Balan, W. S.; Janaun, J.; Chung, C. H.; Semilin, V.; Zhu, Z.; Haywood, S. K.; Touhami, D.; Chong, K. P.; Yaser, A. Z.; Lee, P. C.; et al. Esterification of residual palm oil using solid acid catalyst derived from rice husk. *J. Hazard. Mater.* **2021**, *404*, 124092.

https://doi.org/10.1021/acsomega.1c05565
ACS Omega 2022, 7, 2786−2797

(56) Kaur, M.; Malhotra, R.; Ali, A. Tungsten supported Ti/SiO2 nanoflowers as reusable heterogeneous catalyst for biodiesel production. *Renewable Energy* **2018**, *116*, 109−119.
(57) Ibrahim, M. L.; Nik Abdul Khalil, N. N. A.; Islam, A.; Rashid, U.; Ibrahim, S. F.; Sinar Mashuri, S. I.; Taufiq-Yap, Y. H. Preparation of Na2O supported CNTs nanocatalyst for efficient biodiesel production from waste-oil. *Energy Convers. Manage.* **2020**, *205*, 112445.
(58) Guan, Q.; Li, Y.; Chen, Y.; Shi, Y.; Gu, J.; Li, B.; Miao, R.; Chen, Q.; Ning, P. Sulfonated multi-walled carbon nanotubes for biodiesel production through triglycerides transesterification. *RSC Adv.* **2017**, *7*, 7250−7258.
(59) Bora, A. P.; Dhawane, S. H.; Anupam, K.; Halder, G. Biodiesel synthesis from Mesua ferrea oil using waste shell derived carbon catalyst. *Renewable Energy* **2018**, *121*, 195−204.
(60) Nongbe, M. C.; Ekou, T.; Ekou, L.; Yao, K. B.; Le Grognec, E.; Felpin, F. X. Biodiesel production from palm oil using sulfonated graphene catalyst. *Renewable Energy* **2017**, *106*, 135−141.
(61) Long, Y. D.; Fang, Z.; Su, T. C.; Yang, Q. Co-production of biodiesel and hydrogen from rapeseed and Jatropha oils with sodium silicate and Ni catalysts. *Appl. Energy* **2014**, *113*, 1819−1825.

https://doi.org/10.1021/acsomega.1c05565
ACS Omega 2022, 7, 2786−2797